IEEE

Coding Metasurface Integrated Dual-band Antenna for Vehicular Communications

IEEE Transactions on Vehicular Technology.

Corresponding author: Zhicheng He
phone :+86 186 0772 0701
Email: hezhicheng815@163.com

Coding Metasurface Integrated Dual-band Antenna for Vehicular Communications

Peiwen Chu, Xuezhi Zheng, *Member, IEEE*, Zhicheng He, Eric Li, Vladimir Volski, *Member, IEEE*, Zhensheng Chen and Guy A. E. Vandenbosch, *Fellow, IEEE*

***Abstract*—This paper presents an ultracompact dual-band vehicular antenna for simultaneous satellite, terrestrial and in-car communications. The antenna consists of 16 dual-band units and a double layer coding metasurface (CMS) which can transmit and reflect electromagnetic (EM) waves in the sub-6 GHz and X-band, respectively. The CMS is located underneath the antenna array, which is not only used as the reflector to increase gain and to transform the polarization for the higher frequency band, but also acts as a bandpass lens to realize the beam-forming for the lower frequency band. The proposed antenna has a very low profile (8.5 mm) and the bandwidth is sufficiently large to meet the need of vehicular communications. The simulated and measured results show that the -10 dB impedance bandwidth is from 5.58 to 5.85 GHz for the lower band and is from 9.79 to 10.09 GHz for the higher band. The maximum gain at 9.88 GHz (for satellite), at 5.73 GHz (for terrestrial) and at 5.83 GHz (for in-car) are more than 19.54 dBic., 14.03 dBi and 5.35 dBi, respectively.**

***Index Terms*—coding metasurface, dual-band double-sided antenna, vehicle satellite communications, V2X communications**

I. Introduction

Smart cars, mainly referring to driverless cars, which integrate safety, efficiency, and convenience, are gradually entering people's lives and will play a very important role in Intelligent City Systems [2-4]. Not only are the traditional car manufacturers actively investing in the research and development of smart cars, but also Internet giants, such as Ali, Tencent, and Google, are rapidly progressing in the field of smart cars.

The driverless function of smart cars relies on the coordination of four aspects: environment perception, vehicle communication and data processing, and actuators [6]. Among them, vehicular communication builds a bridge between the vehicle and everything in the world.

Usually, the vehicular communication mainly consists of three parts: satellite communication, terrestrial communication and in-car communication. Satellite communication refers to the information transfer between the car and the satellite, terrestrial communication refers to the communication with surrounding vehicles and roadside units (RSU), and in-car communication refers to devices inside the car. On the one hand, in-car communication can optimize the audio-visual entertainment experience of passengers in the vehicle. On the other hand, more importantly, it also provides a platform for the installation of more in-depth smart technologies such as in-car smart butlers [8], health monitoring [10] and gesture recognition [11] in the future.

In practical applications, since the space in a car is limited, and the number of antennas that need to be installed in the car has increased exponentially in recent years, both the industrial and academic communities tend to reduce the number of antennas by designing multi-band antennas, thereby saving space and cost. In recent years, many dual-frequency or multi-frequency antennas in automobiles have been reported [1, 5, 12-15]. For instance, in [12], a dual-band linearly polarized (LP) antenna is proposed. By stacking two different metal patches, two radiation patterns with a broadside beam and a conical beam are generated in different bands, which are used for satellite and base station communications, respectively. For the same application scenario, [1] proposed another solution, a dual-band circularly polarized (CP) all-metal antenna. The antenna emits left-handed and right-handed circularly polarized (LCP and RCP) waves at two working frequencies for simultaneous satellite and base station communications. Thanks to two different circular polarizations, this design has less coupling between the channels compared with [12]. Further, in [5] , the authors propose another design. There, the antenna works in two frequency bands. For both bands, the antenna transmits via the LCP wave and receives via the RCP wave, which further improves the band utilization and reliability of the antenna.

The project is supported by the Foundation for Innovative Research Groups of the National Natural Science Foundation of China (Grant No. 51621004) and the Natural Science Foundation of China (Grant No. U1864207), the Opening Project of the Guangxi Key Laboratory of Automobile Components and Vehicle Technology of Guangxi University of Science and Technology (No. 2017GKLACVTKF01), and Peiwen Chu was supported by the China Scholarship Council for 2 years study at the Katholieke Universiteit Leuven. (*Corresponding author: Zhicheng He*)

P. Chu, Z. He are with the State Key Laboratory of Advanced Design and Manufacturing for vehicle Body, the college of Mechanical and Transportation Engineering, Hunan university, Changsha, 410082, China. (e-mail: Jacpainechu@hnu.edu.cn, hezhicheng815@163.com)

Eric Li is with School of Computing, Engineering & Digital Technologies, Teesside University, UK (email: ericsg2012@gmail.com)

X. Zheng, V. Volski, Z. Chen and G.A.E. Vandenbosch are with the with the ESAT-WaveCoRE Research Division, Department of Electrical Engineering, KU Leuven, 3001 Leuven, Belgium. (e-mail: Xuezhi.Zheng@esat.kuleuven.be, Vladimir.Volski@esat.kuleuven.be, Zhensheng.Chen@esat.kuleuven.be, Guy.vandenbosch@kuleuven.be).

In general, to achieve the above-mentioned functions, on the one hand, a more complicated feeding network is required which increases the costs, and on the other hand, the thickness of the antenna is often relatively large. Its installation on the roof of the car will not only affect the appearance but also weaken the aerodynamic performance. In order to reduce the cost and the profile, many works based on, e.g., planar array antennas, matching radomes, reflectors, have been reported [7, 9, 16-20]. In [17], a radome was proposed. By adding split ring slots on a frequency selective surface (FSS), a simultaneous absorption of the horizontally polarized waves and transmission of the vertically polarized waves is realized. In [7], an array of antennas with a simple feeding network is placed on top of a multilayer structure. This multilayer structure consists of, from top to bottom, an artificial magnetic conductor (AMC), a FSS, and another AMC. The FSS composes of two layers of loop-shaped elements with an air gap in-between. The antenna array emits LP waves in two frequency bands. In the lower frequency band, the LP waves transmit through the top AMC and the FSS but are reflected by the bottom AMC and converted to LCP waves. In the higher frequency band, the LP waves get immediately reflected by the top AMC and are converted to RCP waves. In this way, a vehicle-mounted dual-band antenna with *a simple feeding network*, that can transmit the positioning signal, while receiving the broadcasting signals from a satellite, is realized. But this design has two disadvantages. One is that the multi-layer structure significantly increases the overall thickness of the system. More importantly, the second is that the design is much complicated by the fact that the top AMC, the bottom AMC and the sandwiched FSS must be tuned altogether to realize the dual-band dual-circularly polarized radiation. In [9], a monopole antenna together with an underneath dielectric is placed on top of a dual-layer FSS with an air gap in between. The FSS consists of a patch layer and a layer composing of complementary split ring resonators (CSRRs), with a sandwiched dielectric. The antenna is fed by a coaxial cable. The incident wave irradiated by the antenna excites two cavity modes supported by the FSS. The bianisotropy of the CSRRs enables the excited cavity modes to satisfy the conditions which allow the dual band radiation of a circularly polarized wave. In this way, a dual band dual CP system with a simple one-port feeding is realized.

A metasurface (MS) is an artificial ultrathin 2-dimensional structure with unit cells small compared to the operating wavelength [21]. It can be used for beamforming, energy harvesting, and EM field manipulation functions [22]. By designing these thin and light EM wave control devices, it is possible to reduce the size and the cost of a system. This idea is gradually applied to microwave [23-27], optical [28, 29] and even acoustic problems [30].

However, designing a metasurface is not easy. The design of the constitutive elements and their arrangement in a metasurface is a complex multivariable optimization problem, which requires considerable computing resources. To simplify the design process, in 2014 the concept of a coding metasurface (CMS) was proposed [31], implementing digital coding inside the MS elements [32]. Using this technique, an n-bit binary number is made to correspond to the phase of the element. The total phase variation, i.e., 360 degrees, in this way can be divided into 2^n steps, and a phase control as fine as $360/2^n$ degrees can be realized. The hardware implementation can be done in various ways, e.g., by using PIN diodes [33], varactor diodes [34], and liquid crystals [35].

CMS can be considered as a very promising technique to reconfigure structures. That is, different functionalities can be implemented by using different binary codes that reconfigure the structure appropriately. The reuse of the same MS design for different scenarios is thus possible.

In this paper, a dual-band multi-function antenna with a low profile and high gain integrated with a CMS is proposed. By multi-function, we mean that this antenna realizes satellite, terrestrial and in-car communications at the same time. The antenna mainly consists of two parts. The first part is a dual-band double-sided LP dipole array, operational in the 5.82 GHz band and at 9.88 GHz. Below the antenna, a multi-functional CMS with 4×8 unit cells is placed. As shown in Fig. 1, the antenna is mounted on the roof of the car. At 5.82 GHz, on the one hand, the double-sided antenna can directly radiate EM waves to the outside of the car for terrestrial communications. On the other hand, the EM waves that are radiated by the array pass through the metasurface and split into 2 beams or 4 beams for in-car communications. In addition, at 9.88 GHz, the MS acts as a reflector and transforms the polarization of the antenna from linear polarization to circular polarization for the satellite communication. Comparing with previous work such as [7] and [9], our antenna realizes more functions and is ultra-compact. The rest of this article is arranged as follows: Section 2 introduces the structure and describes the design process of each part of the antenna. The performance optimization and experimental verification are given in Section 3.

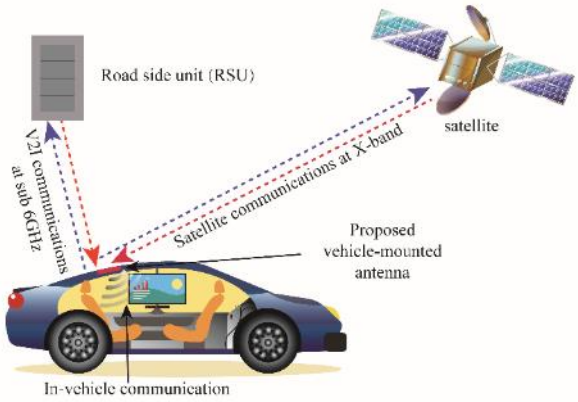

Fig. 1. Schematic diagram of the working scene of the antenna.

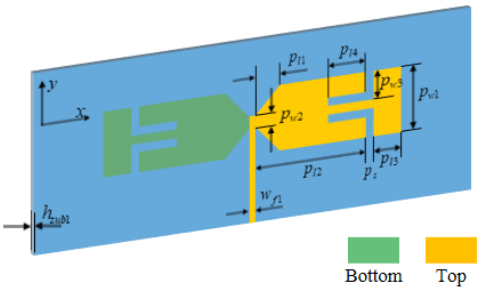

Fig. 2. Double-sided dipole array element.

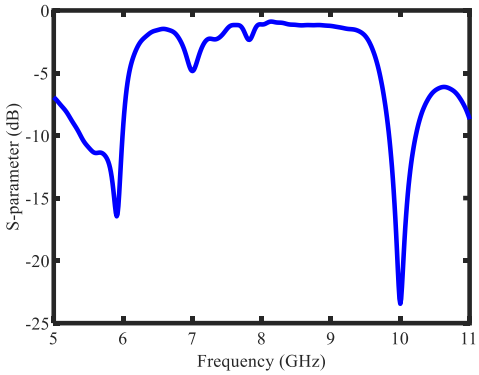

Fig. 3. Reflection coefficient of the double-sided dipole antenna element.

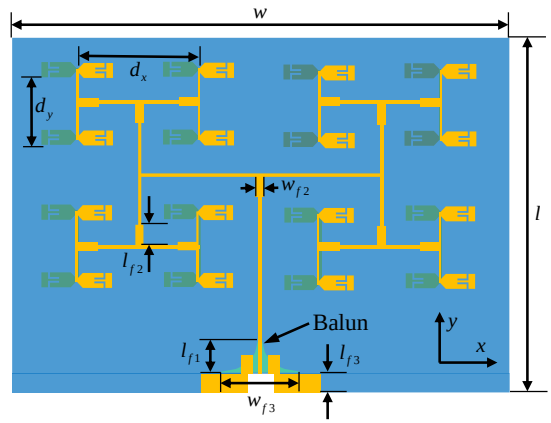

Fig. 4. configuration of the 16-element antenna array.

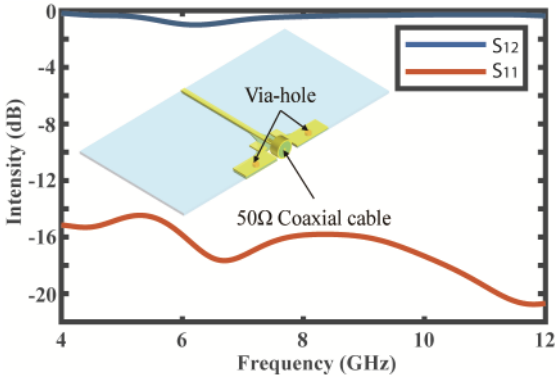

Fig. 5. The balun (the inset), the simulated S11 (red solid curve) and the simulated S12 (blue solid curve).

II. Design of the Antenna

A. Dual-band Double-sided Array

The configuration of the double-sided dipole element is shown in Fig. 2. This antenna topology has been discussed in detail in previous works [7, 36]. We use this well-known topology [28] and tune the geometry and the material. In short, the antenna consists of a dipole with two arms. The arms are printed on opposite sides of the substrate. The antenna is fed by a balanced transmission line. The arm of the dipole takes a bow tie-shape, and two L-shaped slots are added to generate a second working frequency band. The substrate used in this paper is Rogers 4350B ($\varepsilon_r = 3.66, \tan\delta = 0.0037$) with a thickness of 0.254 mm. The reason for choosing such a thin substrate is to reduce the phase difference between the arms on both sides, thereby ensuring the consistency of the radiation pattern on both sides. The simulated reflection coefficient is shown in Fig. 3. The two resonant frequencies at 5.9 GHz and 10 GHz can be clearly observed.

TABLE I
DIMENSIONS OF THE PROPOSED ANTENNA ARRAY

Parameter	Value (mm)	Parameter	Value (mm)	Parameter	Value (mm)
l	115.4	w	192	p_{l1}	0.5
l_{f1}	10.25	w_{f1}	0.5	p_{l2}	7.7
l_{f2}	3.56	w_{f2}	0.88	p_{l3}	2.6
l_{f3}	4.4	w_{f3}	20.5	p_{l4}	4
d_x	30	p_{w1}	4.85	p_s	0.2
d_y	24	p_{w2}	0.56		
h_{sub1}	0.254	p_{w3}	1.26		

The 16-element array formed with this element is shown in Fig. 4. All design parameters are listed in Table I. The size of the array is $w \times l = 192\ \text{mm} \times 115.4\ \text{mm}$. The distance between two dipoles is 30 mm in the x direction (see d_x in Fig. 4) and 24 mm in the y direction (see d_y in Fig. 4). The spacing in the y-direction is consistent with the period of the MS (MS will be detailed in the next section) in the y-direction so that the interaction between an element in the array and a corresponding unit cell in the MS is maximized. To reach an optimal impedance matching, we add rectangular patches with a size of $w_{f2} \times l_{f2}$ at the intersection between the transmission line and the balun at the feeding position. The balun, its S_{11} and S_{12} are shown in Fig. 5. The S_{11} is lower than -10 dB from 4 to 12 GHz. At this point, an antenna that meets our requirements has been designed.

B. Coding Metasurface

The MS consists of 2 substrates (see substrate 1 and 2 in Fig. 6(a)) and 4 metal layers (the receiving layer, the DC feeding, the ground and the radiating layer in Fig. 6(a)). Substrate 1 and Substrate 2 are RO4003C ($\varepsilon_r = 3.55,\ \tan\delta = 0.0027$) with a thickness of 1.524 mm. Substrate 1 is glued to the ground by a Bondply (i.e., Ro4450F with $\varepsilon_r = 3.52$) with a thickness 0.1 mm.

The receiving layer (see Fig. 6(a)) is etched on top of substrate 1. The unit cell of the receiving layer consists of two types of elements (see Fig. 6(c)). The first type consists of

TABLE II
DIMENSIONS OF THE PROPOSED CODING METASURFACE

Parameter	Value (mm)	Parameter	Value (mm)	Parameter	Value (mm)
p	24	a_1	*16*	d_1	*6.5*
s_1	0.2	a_2	*6.5*	d_2	*1.6*
s_2	0.8	b_1	*13*	d_3	*12.8*
h_b	0.1	b_2	*9.3*	d_4	*3*
h_{sub2}	1.524	c_1	*1~2.2*	t	*0.035*
r_1	0.9	c_2	*2.3*		
r_2	1.2	c_3	*5.1*		

square patches with rounded corners (see the "large period" element positioned at the center of the dual-band element in Fig. 6(c)). This unit cell has a period of 24 mm and operates at 5.82 GHz. The second type consists of small squares with dented corners (see the "small-period" element positioned at the corners of the dual-band element in Fig. 6(c)). This unit cell has a period of 12 mm and operates at 9.88 GHz.

The DC feeding layer is etched at the bottom of substrate 1. It is noted that the DC feeding does not play a significant role on the response of the MS. To confirm this, simulations have been done for the cases where the feeding is deleted or is shifted to another position. It is seen from Fig. 7 that the magnitudes of the reflection and transmission coefficients are not significantly affected.

Through the via-hole 2 (see Fig. 6(a)), the large-period element at the center of the dual-band element is connected to the DC feeding layer. The DC current passes through the via-hole 1 on the receiving layer, through substrate 1, Bondply, ground, and substrate 2, and is connected to the T-shaped patch (see Fig. 6(b)) at the center of the radiating layer. The hollow oval patch (see Fig. 6(b)) on this layer is further connected to the T-shape patch through the diodes. The diode used in this article is MACOM MA4SPS402 ($C_t = 0.045$ pF and $R_s = 5\,\Omega$). Lastly, the whole system is grounded by symmetric via-holes, i.e., via-hole 3 and 4. All the geometric parameters about the metasurface are listed in Table II.

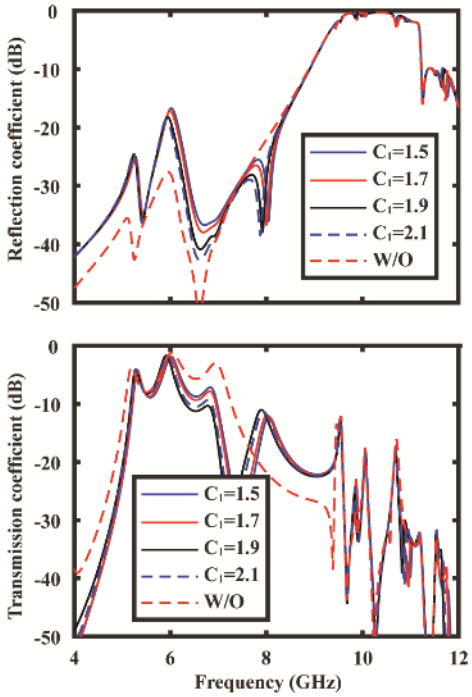

Fig. 7. Influence of the DC feeding on the response of the MS. Transmission and reflection coefficients for the different DC feedings are shown in the top and the bottom panels. The red dashed line gives the magnitude of the reflection and transmission without (i.e., W/O in the figure) the DC feeding. The solid blue, solid red, solid black, and dashed blue lines give the results for C_1=1.5, 1.7, 1.9, and 2.1 mm, respectively. C_1 is the length between the via hole 2 and the DC feeding (see Fig. 6(b)).

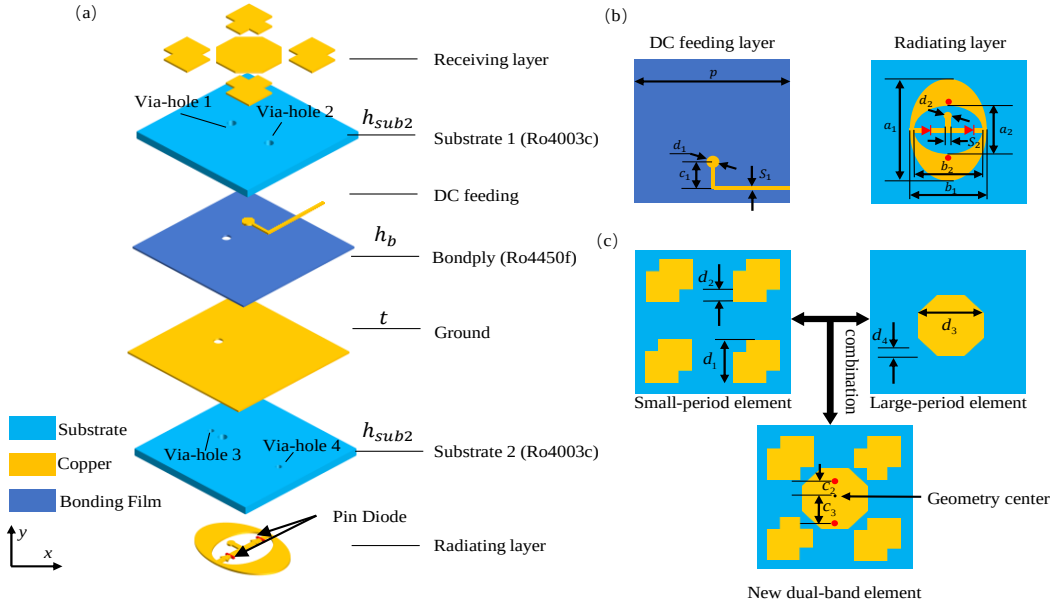

Fig. 6. Topology of a unit cell of the proposed coding metasurface. (a) Exploited view of the unit cell. The radiating layer and the receiving layer are connected by the via-hole 1. The DC feeding is connected to the receiving layer by via-hole 2. The via-hole 3 and 4 are used to link the radiation layer with the ground. (b) The schematics of the DC feeding and radiation layer. (c) The "divide-and-rule" strategy. The new dual-band element is formed by combining the small-period element at 10 GHz with the large-period element at 5.82 GHz.

It should be emphasized that it is challenging to realize multiple functions at the same time through one compact structure. To achieve this, we adopt a "divide-and-rule" design strategy (see Fig. 6(c)). In this approach, in the first iteration, the large-period and the small period elements are designed separately for lower and higher frequencies (See Appendix A for the separate designs). After that, they are combined in a later stage to form the dual-band element in the final MS layout.

Then, first, the CMS transmits at 5.82 GHz. This can be seen from Fig. 8(a) that at 5.82 GHz, the transmission coefficient peaks with a bandwidth of 0.2 GHz. By further controlling the direction of the DC currents, the states of the diodes on the radiating layer, i.e., the "on" and "off" states, can be tuned. The direction of the currents on the radiation layer is shown in Fig. 9. This allows us to adjust the radiation pattern to suit different cars.

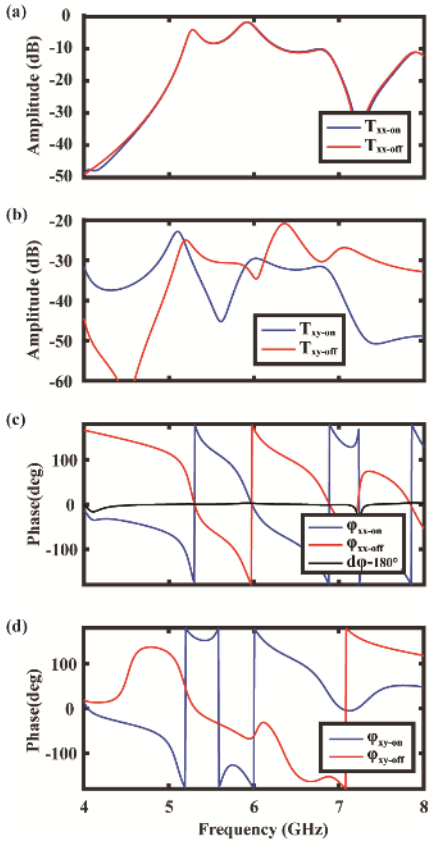

Fig. 8. Amplitude (the first two panels) and phase (the last two panels) of the transmission coefficient for the "on" (in red) and "off" (in blue) states of the diode. In (a) and (c), the co-polarization case is shown, while, in (b) and (d), the cross-polarization case is shown. The black line in (c) is obtained in two steps. In the first step, we calculate the difference between the phase of the "on" state transmission coefficient and the phase of the "off" state transmission coefficient. In the second step, we subtract 180 degrees from the difference obtained in the first step and plot the black line.

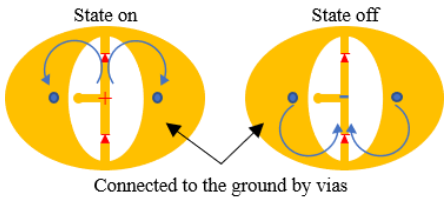

Fig. 9. Schematics of the currents on the radiating layer under different states of the diode.

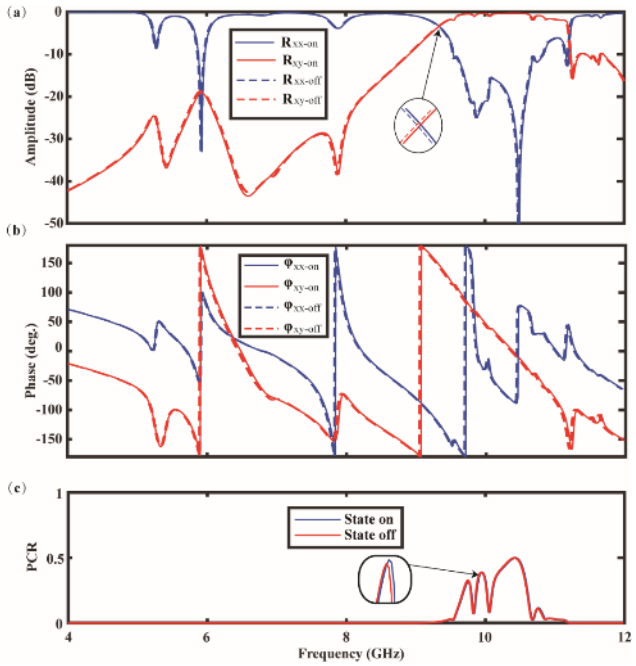

Fig. 10. Amplitude (a) and phase (b) of the reflection coefficient for the "on" (solid line) and "off" (dashed line) states of the diodes. Red is used for the cross-polarization and blue is used for the co-polarization. In (c), the PCRs defined as $|R_{xy}|/(|R_{xx}|+|R_{xy}|)$ under state on (blue) and state off (red) are shown. The fact that the dashed lines coincide with the solid lines shows that the influence of the state of the diode is insignificant.

Second, at the frequencies other than 5.82 GHz, the CMS functions as a reflector. Especially, it is seen from Fig. 10(a) that the cross-polarization reflection coefficient maximizes around 10 GHz with a bandwidth of 1.8 GHz and reaches a polarization conversion rate (PCR) close to 100% (see Fig. 10(c)) between 9.6 and 10.6 GHz. By further adjusting the distance between the antenna array and the MS, the phase difference between the reflected wave and the wave directly radiated by the antenna can be modified to 90 degrees or 270 degrees (see Fig. 10(b)). Hence, the CMS reflects and transforms the LP wave generated by the antenna into a CP wave around 10 GHz and can be used for the satellite communication.

As a remark, it is noted that the effects of the "on" and the "off" states of the diode do not have a significant impact on the response of the MS. This can be seen from Fig. 8 and Fig. 10 that the amplitude and the phase of the reflection coefficients are almost identical for both states. For the transmission coefficient, the phase difference between the two states remains 180 degrees over the entire band (see the black line in Fig. 8(c)) which can be beneficial for tolerating fabrication errors, and provides an ideal platform for realizing multi-functions, while the amplitudes of the two states are again almost indistinguishable.

C. *Co-design of array and metasurface*

The entire system, where the MS is placed under the antenna, is shown in Fig. 11. Support and fixation are provided through 4 circular holes. The holes are drilled in the MS and the antenna. Via the holes, a spacer, i.e., a polystyrene foam (whose dielectric constant is around 1.1), is inserted between the MS and the antenna.

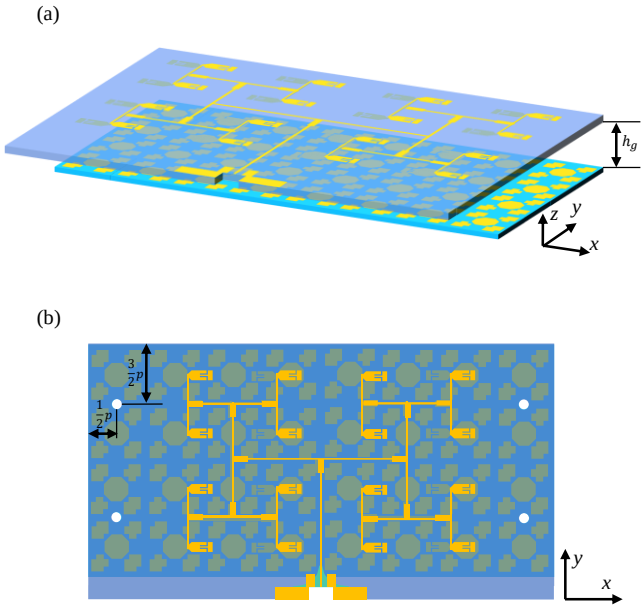

Fig. 11. Perspective view (a) and top view (b) of the antenna system.

Further, it is found that the optimal distance between the antenna and the MS is 5 mm (see details in Appendix B). It is worth noting that the total thickness of the antenna including the gap is then less than 9 mm, which is much thinner than other multi-functional antenna designs working in the same band (e.g., [7]). To be complete, we show in Fig. 12 that the effects of the spacer on the performance of the entire system.

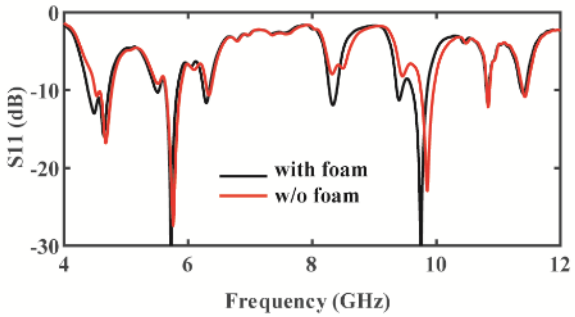

Fig. 12. Effects of the foam on S_{11} (at the port of the coaxial cable) of the co-design.

At 5.82 GHz, to realize the real-time control of the radiation pattern, we tune the diodes within each MS unit cell. Fig. 13 (a) and (b) show two "codes", where red indicates the "on" state, and black does the "off" state. Fig. 13 (c) and (d) demonstrate the radiation patterns due to the "coding". It is observed that the beam is split into 2 and 4 sub-beams by the MS. As a remark, it is noted that although the codes are distributed symmetrically as in Fig. 13(a), the beams are asymmetrical. This is due to the fact that the double-sided antenna does not hold reflection symmetries (see the antenna layout in Fig. 2 and Fig. 4), which results in asymmetries in both the far and near fields (see Fig. 14) of the antenna. Further, the receiving layer of the MS is lack of symmetries (see the small period elements in Fig. 7(b)). The symmetries in the beams may be realized by a systematic use of symmetric antenna and MS elements, or the same antenna array but a much larger MS with more controllable elements so that more sophisticated codes can be implemented to correct the uneven beams. The research on this aspect will be delayed to our future works.

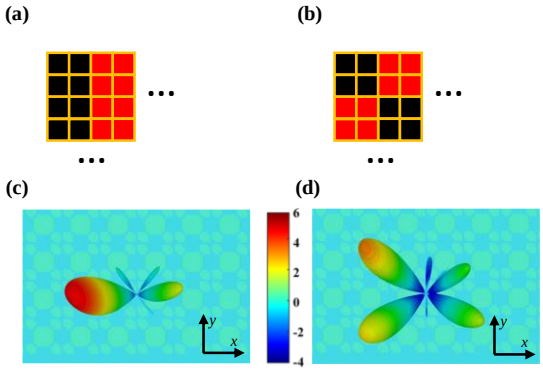

Fig. 13. Beamforming by programming the CMS. (a) and (b) show two configurations of the diode states: red is for "on", while black is for "off". (c) and (d) demonstrate the radiation patterns of the two configurations. The colors of (c) and (d) are coded from blue to red to the strength of the radiation (see the color bar between (c) and (d)).

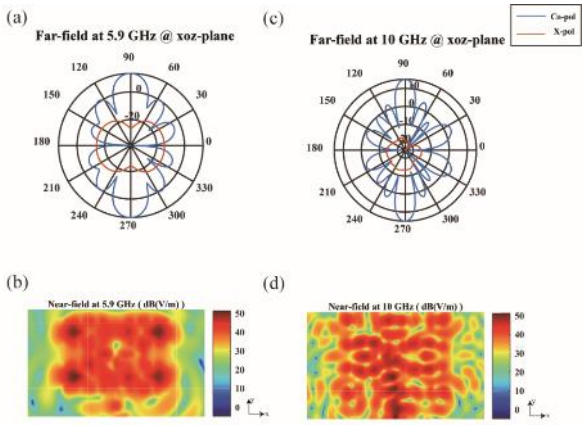

Fig. 14 The simulated far-field patten and near-field distribution radiated by the antenna array (without the MS) at 5.9 GHz and 10 GHz.

III. Results and Discussions

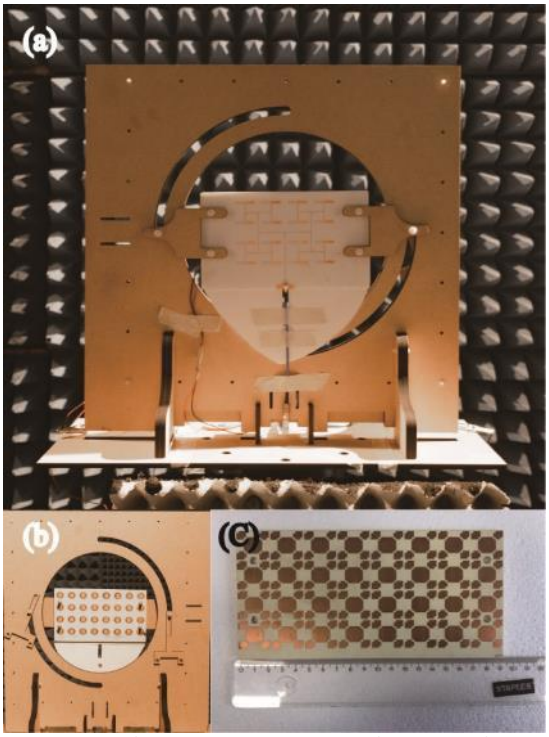

Fig. 15. Prototype of the proposed antenna: (a) front view of the antenna array with the holder. (b) back view (i.e., the radiating layer) of the antenna and (c) the receiving layer of the metasurface.

To verify the proposed design, a prototype (see Fig. 15) was fabricated (the machining accuracy is 0.15 mm) and measured. The simulated and measured S-parameters are shown in Fig. 16. For the sub-6 GHz band, the −10 dB impedance bandwidth is from 5.58 GHz to 5.85 GHz, and for the X-band, the −10 dB impedance bandwidth is from 9.81 GHz to 10.08 GHz.

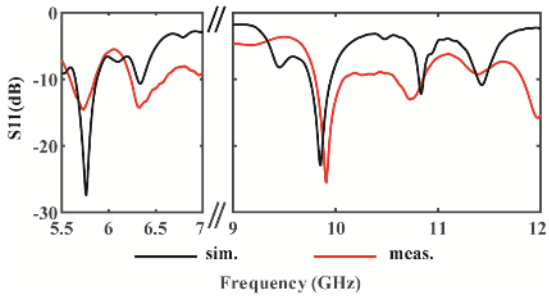

Fig. 16 Simulated and measured S-parameter of the antenna.

Further, the simulated and the measured radiation patterns are shown in Fig. 17. Fig. 17(a)-(b) and Fig. 17(c)-(d) show the co-polarization (abbreviated as "Co-pol" in Fig. 17, i.e., the direction of the radiated electric field being parallel with the direction of the main axis of the antenna, see the *x* axis in Fig. 4), and cross-polarization (abbreviated as "Cross-pol", i.e., the direction of the radiated electric field being perpendicular to the direction of the main axis of the antenna, see the *y* axis in Fig. 4) at 5.82 GHz and 9.88 GHz, respectively. It can be observed that at 5.82 GHz, the antenna directly radiates a co-polarized wave to the upper half-space (that is, the space outside the car), forming a wide beam in the main polarization direction (see the shaded region in Fig. 17(a)), with a gain of 14.03 dBi, which can be used for the terrestrial communication. For the lower half-space (that is, the interior space of the car), the wave radiated by the antenna is incident upon the metasurface, is transformed into a cross-polarized wave by the radiating layer (see a further explanation in Appendix C) and is split into two beams that can be respectively directed to the front and rear seats in the cockpit (see the two shaded regions in Fig. 17(b)). The gain reached more than 5.35 dBi for the beam to the front seats and 2.21 dBi for the beam to the back seat. At 9.88 GHz, a 19.54 dBic circularly polarized beam is generated in the upper half of the space (see the shaded region in Fig. 17(c) and (d) in dBi and Fig. 18(a) in dBic), which is for satellite

TABLE III: COMPARISON OF DIFFERENT VEHICULAR ANTENNAS

Ref.	Antenna Type	Working band (GHz)	Size (λ_0)	Peak (dBic)	AR Bandwidth (%)	Elements in array	Realized function
[1]	all-metal antenna	2.4-2.61 2.64-3.00	0.62×0.62 ×0.14	5.35 5.76	0.7 0.68	-	Satellite communication; Terrestrial communication
[5]	cavity backed antenna	1.055-1.325 1.54-1.63	0.78×1.011 ×0.22	9 9.53	3.91 7.4	-	Satellite communication; Terrestrial communication
[7]	Patch antenna integrated FSS and AMC	7.8-8.5 14-15.3	2.9×1.74 ×0.58	16.1 15.2	3 4.1	4×7	Satellite communication
[9]	Patch antenna integrated metasurface	1.8-1.94 2.23-2.53	0.33×0.33 ×0.04	3.95 5.29	2.67 2	2×2	Satellite communication; Terrestrial communication
This work	Patch antenna integrated metasurface	5.58-5.85 9.81-10.08	3.84×2.22 ×0.17	14.03 (dBi) 19.54	- 2.5	4×8	Satellite communication; Terrestrial communication; In-car communication

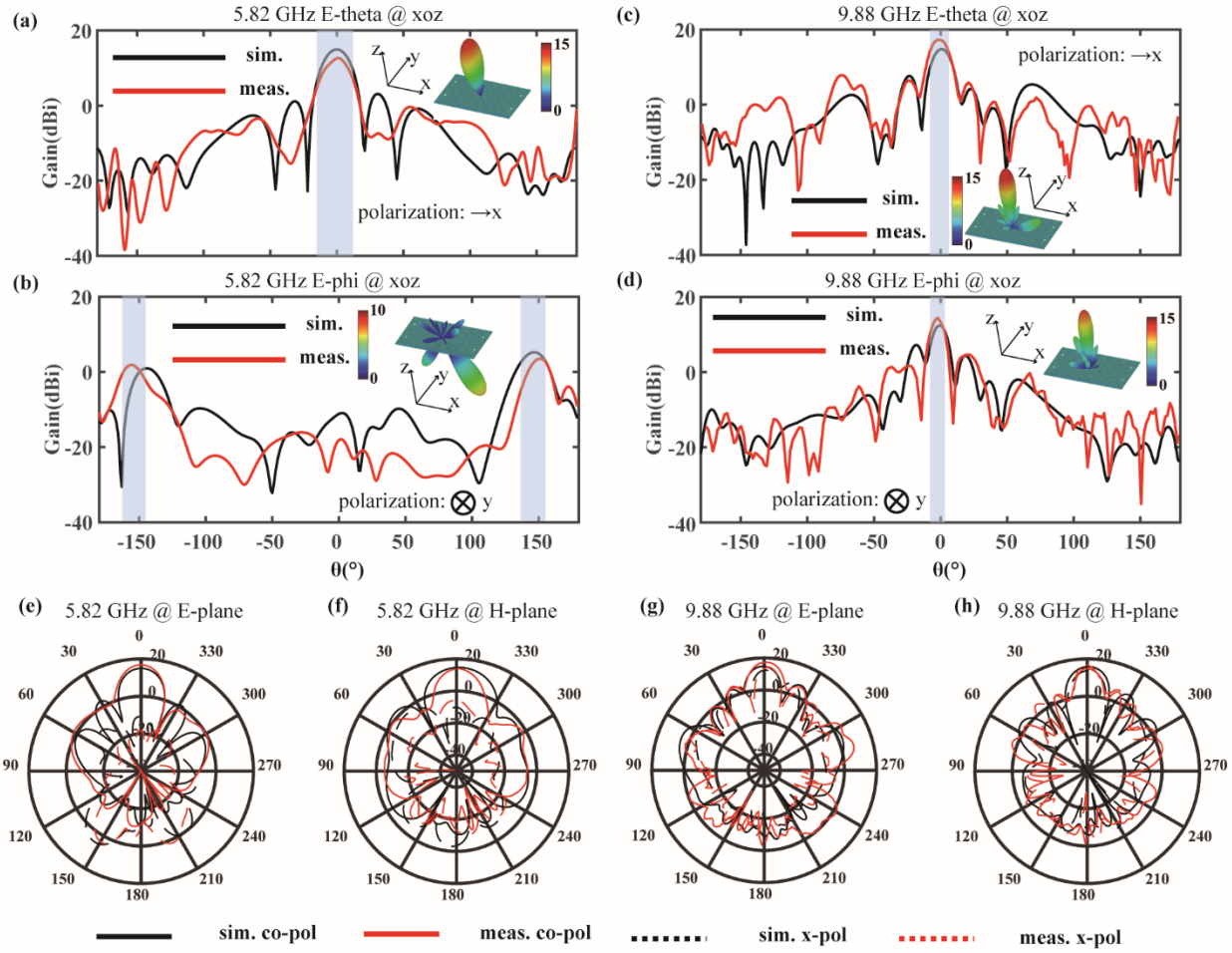

Fig. 17. Simulated and measured radiation patterns of the array at 5.82 GHz ((a) E-theta, (b) E-phi, (e) E-plane and (f) H-plane) and at 9.88 GHz ((c) E-theta, (d) E-phi, (g) E-plane and (h) H-plane), respectively. The polarization directions of (a) and (c) are along the x-axis (see the insets of (a) and (c)), and the polarization directions of (b) and (d) are along the y-axis (see the insets of (b) and (d)).

communications. The measured 3-dB axial ratio in terms of the frequency is shown in Fig. 18(b). The aperture efficiency of the antenna is 22% and 20% at 5.82GHz and 9.88GHz, respectively. The efficiency is low due to the high loss in the active devices, which is very common in reconfigurable metasurfaces (e.g., 12.84% in [37], 17.9% in [38] and 13.2% in [39]). The radiation efficiencies are 91.39% and 82.56% at 5.82 GHz and 9.88 GHz, respectively. For the sake of completeness, the radiation efficiencies (without the MS) are also given: they are 94.32% and 89.34% at 5.82 GHz and 9.88 GHz, respectively.

Table 3 compares the antenna proposed in this article with other dual-band antennas in literature. As can be seen, in [9], the all-metal antenna has a low profile (which requires high accuracy when manufacturing and thus increases the cost), but the AR bandwidth is too narrow compared to this work. The antenna in [10] is excellent in performance, but it has a very complex feeding network. Compared with [9] and [10], [17] has a simple feeding network and wider bandwidth. However, to increase the bandwidth, in [17] multiple air gaps have been added between the components, thereby increasing the overall thickness. In [20], the profile is reduced while ensuring a good bandwidth. Through a structural design, the antenna in [20] can excite two vertical modes through a single feed to generate circular polarization. However, the antenna proposed in this paper, having a good bandwidth, gain and compact profile, realizes an additional function: in-car communication, on top of [20] which only reports the satellite and the terrestrial communications.

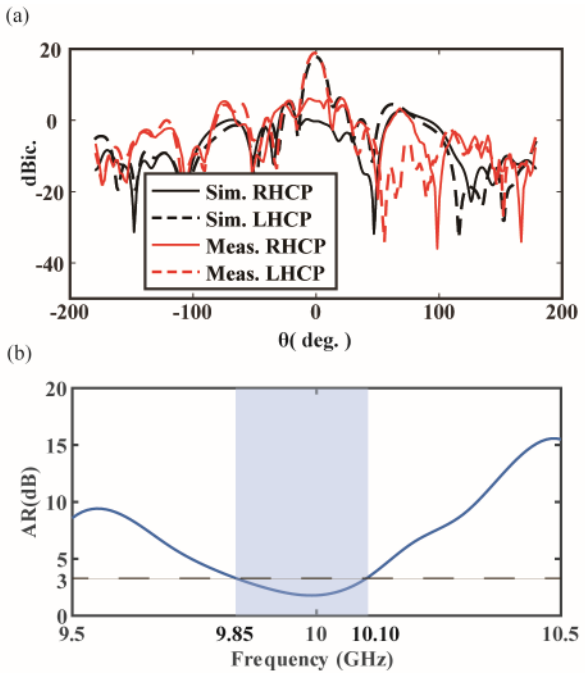

Fig. 18. (a) LCP and RCP gains and (b) Measured 3-dB axial ratio versus frequency. The shaded part highlights the 3 dB AR bandwidth.

IV. Conclusions

A multi-functional dual-band double-sided antenna is proposed. This antenna consists of two parts, a dual-band double-sided linear polarization array and a coding metasurface. Thanks to the coding metasurface, the antenna realizes beamforming and polarization conversion of EM waves at 5.82 GHz and 9.88 GHz, respectively. At 5.82 GHz, the maximum gains in the upper and lower half space are 14.03 dBi and 5.35 dBi, respectively, which is suitable for communication outside/inside a car. At 9.88 GHz, a circularly polarized beam with a gain of 19.54 dBic is realized with an axial ratio bandwidth of 0.25 GHz (2.5%), which can be used for satellite communication. The main advantages are thus the multiple functions for an ultra-thin structure of less than 9 *mm*.

Appendix A: Design of Small-Period and Large-Period Elements in the CMS

In this Appendix, we illustrate the performance for the small-period and large period elements, when they are considered separately. As shown in Fig. A1, the simulation results of the separate design are very similar to the ones when the two elements are considered together (See Fig. 8 and Fig. 10 in the main text). This indicates that the adopted "divide-and-rule" design strategy is correct, which greatly facilitates the targeted MS design.

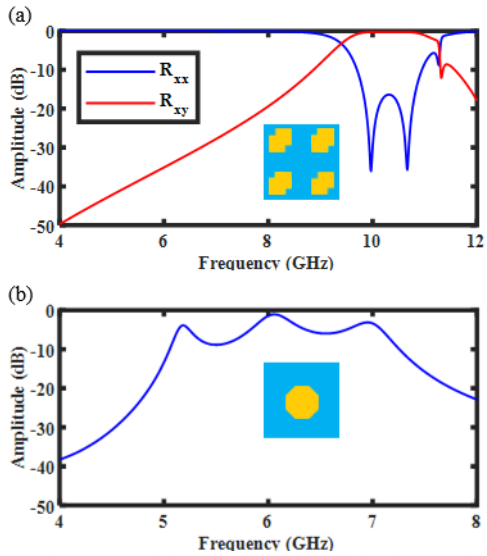

Fig. A1. Performance of the small-period and the large period elements when they are separately considered. The co- (blue) and the cross- (red) polarization reflection coefficients for the small-period elements are shown in (a). The transmission coefficient of the large-period elements is shown in (b).

Appendix B: The Distance Between Antenna Array and Metasurfaces

In this Appendix, we illustrate how the distance between the antenna array and the metasurface is determined. It is noted that the electric field above the system takes the following generic form,

$$\mathbf{E} = E_x e^{-jkz}\mathbf{x} + R_{xx}e^{-j\varphi_{xx}} \cdot E_x e^{-jkz}\mathbf{x} + R_{yx}e^{-j\varphi_{xy}} \cdot E_y e^{-jkz}\mathbf{y}. \quad (1)$$

In Eq. (1), **x** and **y** are unit vectors along the *x* and the *y* directions. On the right-hand side (RHS) of Eq. (1), the first term denotes the direct radiation from the antenna array. The second and the third terms mark the waves reflected by the MS. To achieve high-quality circular polarization performance, on the one hand, it is necessary to ensure that the second term on

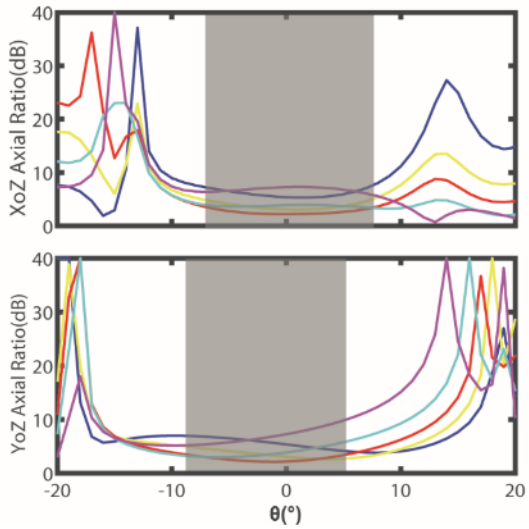

Fig. A2. Simulated axial ratio (AR) in the *XoZ*-plane and the *YoZ*-plane for different spacings between the antenna and the metasurface. The solid blue, yellow, red, cyan, and magenta lines denote the ARs at $h_g = 3, 4, 5, 6$ and 7 *mm*, respectively. The shaded region marks the range where the AR is lower than 3dB for the case $h_g = 5$ *mm* (i.e., the red line).

the RHS of Eq. (1), i.e., R_{xx}, is as small as possible, thanks to the high polarization conversion efficiency at 9.88 GHz of the MS design in Section II.B (see the lower panel in Fig. 10), the first condition is easily satisfied. On the other hand, $\varphi_{xy} + 2kh_g$ is to assure a 90-degree phase difference between the field radiated by the antenna and the field reflected by the CMS. For this, we tune the distance between the antenna array and the MS. In the design, we read that the phase of the reflection coefficient φ_{xy} off Fig. 10, calculate h_g and find that h_g being less than 7.5mm. After setting this upper bound, we run a parameter scan to determine the optimal distance where the axial ratio is the best. The change of the axial ratio (AR) with the distance is shown in Fig. A2. It is seen that for $h_g = 5\ mm$, the optimal AR is achieved.

APPENDIX C: THE CURRENT ON THE RADIATING LAYER OF THE METASURFACE

Here, we further explain the polarization conversion, i.e., the "Cross-pol" component in Fig. 17(b), at lower band, i.e., 5.82 GHz, by showing the current distribution on the radiating layer (see Fig. 6(a) and (b)). As shown in Fig. A3, the current on the radiating layer mainly flows along the *y*-direction (see the coordinate system in Fig. A3 below). Hence, the polarization of the split beams (e.g., the shaded regions in Fig. 17(b)) as a result of the radiation of the current is dominated by the *y*-component, i.e., the "Cross-pol" component.

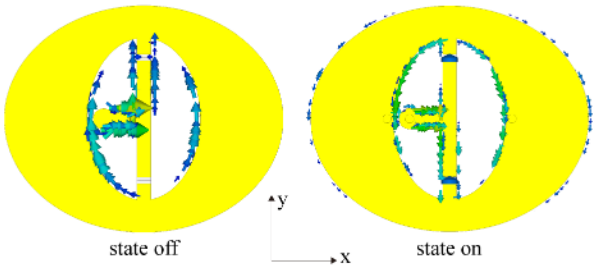

Fig. A3. The current distribution on the radiating layer of the metasurface.

REFERENCES

[1] S. Wang, L. Zhu, G. Zhang, J. Yang, J. Wang, and W. Wu, "Dual-band dual-CP all-metal antenna with large signal coverage and high isolation over two bands for vehicular communications," *IEEE Transactions on Vehicular Technology,* vol. 69, no. 1, pp. 1131-1135, 2019.

[2] H. Liu *et al.*, "A review of the smart world," *Future generation computer systems,* vol. 96, pp. 678-691, 2019.

[3] K. Shafique, B. A. Khawaja, F. Sabir, S. Qazi, and M. Mustaqim, "Internet of things (IoT) for next-generation smart systems: A review of current challenges, future trends and prospects for emerging 5G-IoT scenarios," *Ieee Access,* vol. 8, pp. 23022-23040, 2020.

[4] S. Talari, M. Shafie-Khah, P. Siano, V. Loia, A. Tommasetti, and J. P. Catalão, "A review of smart cities based on the internet of things concept," *Energies,* vol. 10, no. 4, p. 421, 2017.

[5] R. Xu, S. S. Gao, J. Li, K. Wei, and Q. Luo, "A Reconfigurable Dual-Band Dual-Circularly Polarized Antenna for Vehicle Global Navigation Satellite System Application," *IEEE Transactions on Vehicular Technology,* vol. 69, no. 10, pp. 11857-11867, 2020.

[6] M. Shammut, "Driverless Cars Implications: A Literature Review," 2020.

[7] J. Zhu, Y. Yang, S. Li, S. Liao, and Q. Xue, "Dual-band dual circularly polarized antenna array using FSS-integrated polarization rotation AMC ground for vehicle satellite communications," *IEEE Transactions on Vehicular Technology,* vol. 68, no. 11, pp. 10742-10751, 2019.

[8] H. Zemrane, Y. Baddi, and A. Hasbi, "Internet of things smart home ecosystem," in *Emerging Technologies for Connected Internet of Vehicles and Intelligent Transportation System Networks*: Springer, 2020, pp. 101-125.

[9] T. Yue, Z. H. Jiang, and D. H. Werner, "A compact metasurface-enabled dual-band dual-circularly polarized antenna loaded with complementary split ring resonators," *IEEE Transactions on Antennas and Propagation,* vol. 67, no. 2, pp. 794-803, 2018.

[10] H. Zhang *et al.*, "A low-profile compact dual-band l-shape monopole antenna for microwave thorax monitoring," *IEEE Antennas and Wireless Propagation Letters,* vol. 19, no. 3, pp. 448-452, 2020.

[11] H. Ruan and L. Li, "Imaging resolution analysis of single-frequency and single-sensor programmable microwave imager," *IEEE Transactions on Antennas and Propagation,* vol. 68, no. 11, pp. 7727-7732, 2020.

[12] L. Ge, S. Gao, Y. Li, W. Qin, and J. Wang, "A low-profile dual-band antenna with different polarization and radiation properties over two bands for vehicular communications," *IEEE Transactions on Vehicular Technology,* vol. 68, no. 1, pp. 1004-1008, 2018.

[13] Z.-P. Zhong *et al.*, "A compact dual-band circularly polarized antenna with wide axial-ratio beamwidth for vehicle GPS satellite navigation application," *IEEE Transactions on Vehicular Technology,* vol. 68, no. 9, pp. 8683-8692, 2019.

[14] Y.-X. Sun, K. W. Leung, and K. Lu, "Compact Dual Microwave/Millimeter-Wave Planar Shared-Aperture Antenna for Vehicle-to-Vehicle/5G Communications," *IEEE Transactions on Vehicular Technology,* vol. 70, no. 5, pp. 5071-5076, 2021.

[15] M. G. N. Alsath *et al.*, "An integrated tri-band/UWB polarization diversity antenna for vehicular networks," *IEEE Transactions on Vehicular Technology,* vol. 67, no. 7, pp. 5613-5620, 2018.

[16] L. Zhou, Z. Liu, L. Tang, and Y. Pei, "Design and characterization for a high-temperature dual-band radome wall structure for airborne applications," *Materials & Design,* vol. 114, pp. 264-270, 2017.

[17] P. Mei, X. Q. Lin, J. W. Yu, P. C. Zhang, and A. Boukarkar, "A low radar cross section and low profile

antenna co-designed with absorbent frequency selective radome," *IEEE Transactions on Antennas and Propagation,* vol. 66, no. 1, pp. 409-413, 2017.

[18] Z. An and M. He, "Design of a Broadband Radome-Enclosed Dual-Polarization Antenna Array Covering Sub-6 GHz Band with Differential Feeding," *International Journal of Antennas and Propagation,* vol. 2020, 2020.

[19] H. Yang, Y. Fan, and X. Liu, "A compact dual-band stacked patch antenna with dual circular polarizations for BeiDou navigation satellite systems," *IEEE Antennas and Wireless Propagation Letters,* vol. 18, no. 7, pp. 1472-1476, 2019.

[20] Q. Zheng, C. Guo, J. Ding, and G. A. Vandenbosch, "Dual-band metasurface-based CP low-profile patch antenna with parasitic elements," *IET Microwaves, Antennas & Propagation,* vol. 13, no. 13, pp. 2360-2364, 2019.

[21] N. Yu and F. Capasso, "Flat optics with designer metasurfaces," *Nature materials,* vol. 13, no. 2, pp. 139-150, 2014.

[22] C. L. Holloway, E. F. Kuester, J. A. Gordon, J. O'Hara, J. Booth, and D. R. Smith, "An overview of the theory and applications of metasurfaces: The two-dimensional equivalents of metamaterials," *IEEE antennas and propagation magazine,* vol. 54, no. 2, pp. 10-35, 2012.

[23] J. Wang *et al.*, "Metantenna: When metasurface meets antenna again," *IEEE Transactions on Antennas and Propagation,* vol. 68, no. 3, pp. 1332-1347, 2020.

[24] A. A. G. Amer, S. Z. Sapuan, N. Nasimuddin, A. Alphones, and N. B. Zinal, "A comprehensive review of metasurface structures suitable for RF energy harvesting," *IEEE Access,* vol. 8, pp. 76433-76452, 2020.

[25] R. Y. Wu, Y. B. Li, W. Wu, C. B. Shi, and T. J. Cui, "High-gain dual-band transmitarray," *IEEE Transactions on antennas and Propagation,* vol. 65, no. 7, pp. 3481-3488, 2017.

[26] K. T. Pham, R. Sauleau, E. Fourn, F. Diaby, A. Clemente, and L. Dussopt, "Dual-band transmitarrays with dual-linear polarization at Ka-band," *IEEE Transactions on Antennas and Propagation,* vol. 65, no. 12, pp. 7009-7018, 2017.

[27] S. A. Matos *et al.*, "High gain dual-band beam-steering transmit array for satcom terminals at Ka-band," *IEEE Transactions on Antennas and Propagation,* vol. 65, no. 7, pp. 3528-3539, 2017.

[28] J. Li, P. Yu, S. Zhang, and N. Liu, "Electrically-controlled digital metasurface device for light projection displays," *Nature communications,* vol. 11, no. 1, pp. 1-7, 2020.

[29] J. He, T. Dong, B. Chi, and Y. Zhang, "Metasurfaces for terahertz wavefront modulation: a review," *Journal of Infrared, Millimeter, and Terahertz Waves,* pp. 1-25, 2020.

[30] Y. Zhu and B. Assouar, "Multifunctional acoustic metasurface based on an array of Helmholtz resonators," *Physical review B,* vol. 99, no. 17, p. 174109, 2019.

[31] S. Liu *et al.*, "Convolution operations on coding metasurface to reach flexible and continuous controls of terahertz beams," *Advanced Science,* vol. 3, no. 10, p. 1600156, 2016.

[32] T. J. Cui, M. Q. Qi, X. Wan, J. Zhao, and Q. Cheng, "Coding metamaterials, digital metamaterials and programmable metamaterials," *Light: Science & Applications,* vol. 3, no. 10, pp. e218-e218, 2014.

[33] C. Huang, B. Sun, W. Pan, J. Cui, X. Wu, and X. Luo, "Dynamical beam manipulation based on 2-bit digitally-controlled coding metasurface," *Scientific reports,* vol. 7, no. 1, pp. 1-8, 2017.

[34] W. Li *et al.*, "Programmable coding metasurface reflector for reconfigurable multibeam antenna application," *IEEE Transactions on Antennas and Propagation,* vol. 69, no. 1, pp. 296-301, 2020.

[35] Q. Wang *et al.*, "Millimeter‐Wave Digital Coding Metasurfaces Based on Nematic Liquid Crystals," *Advanced theory and simulations,* vol. 2, no. 12, p. 1900141, 2019.

[36] K. Kiminami, A. Hirata, and T. Shiozawa, "Double-sided printed bow-tie antenna for UWB communications," *IEEE antennas and wireless propagation letters,* vol. 3, no. 1, pp. 152-153, 2004.

[37] X. Wan *et al.*, "Reconfigurable sum and difference beams based on a binary programmable metasurface," *IEEE Antennas and Wireless Propagation Letters,* vol. 20, no. 3, pp. 381-385, 2021.

[38] H. Yang *et al.*, "A 1-bit 10x10 reconfigurable reflectarray antenna: design, optimization, and experiment," *IEEE Transactions on Antennas and Propagation,* vol. 64, no. 6, pp. 2246-2254, 2016.

[39] Z. Wang *et al.*, "1 bit electronically reconfigurable folded reflectarray antenna based on pin diodes for wide-angle beam-scanning applications," *IEEE Transactions on Antennas and Propagation,* vol. 68, no. 9, pp. 6806-6810, 2020.